Research Article

Received: 2 July 2018 Revised: 20 September 2018 Accepted article published: 27 September 2018 Published online in Wiley Online Library: 20 November 2018

(wileyonlinelibrary.com) DOI 10.1002/jctb.5835

Evaporation-induced self-assembly (EISA) synthesized mesoporous bimetallic oxides (MBOs) enabling enhanced co-uptake of arsenate and fluoride from water

Feihu Li,* Jingjing Fu, Jie Jin, Silan Wang,# Yangyang Liu, Meng Yang and Xiaoru Fu

Abstract

BACKGROUND: Simultaneous removal of arsenic and fluoride anions from water by adsorption remains a challenge for environmental remediation practice. To address this issue, four mesoporous bimetallic oxides (MBOs) were prepared via the evaporation-induced self-assembly (EISA) method and studied as adsorbents for the co-uptake of arsenate (As(V)) and fluoride (F^-) from synthetic wastewater. Adsorption envelope and equilibrium experiments were performed to investigate the adsorption behaviors and properties.

RESULTS: These composites possessed high surface areas (e.g. 200 $m^2\ g^{-1}$ for meso-Ti/Al) and well-defined mesopores, enabling high adsorption capacities for both As(V) and F^-. The maximum adsorption capacities of mesoporous titanium-lanthanum oxide (meso-Ti/La) were as high as 81.42 mg g^{-1} and 44.37 mg g^{-1} for As(V) and F^-, respectively. Surface complexation modeling indicates that As(V) removal mainly involved bidentate surface complexation with surface ≡Me-OH, while F^- was retained by formation of monodentate surface complexes.

CONCLUSION: The removal mechanisms were confirmed by X-ray photoelectron spectroscopy. These MBOs were found to be effective for simultaneous removal of arsenic and fluoride from water. This study also demonstrated that the incorporation of multi-components and mesoporosity into one composite is an efficient strategy for design and application of high-efficiency adsorbents for environmental remediation of aqueous contaminants.

Supporting information may be found in the online version of this article.

Keywords: adsorption; arsenate; CD-MUSIC; fluoride; mesoporous bimetallic oxides

INTRODUCTION

Co-occurrence of arsenic (As) and fluoride ion (F^-) in both natural aquifers (e.g. groundwater, and mine water) and industrial wastewaters (e.g. effluents from electroplating plants) is found in many countries throughout the world.[1–4] Groundwater with both As and F^- was found in Argentina,[5] China,[6] India,[7] Mexico,[8] and Pakistan,[9] most of which have been suffering environmental and health risks, since co-exposure to As and F^- even at very low concentrations has severely synergistic adverse consequences for animals and/or humans.[10–12] A wide range of point-of-use treatment techniques has been developed in past decades to remove both anions (i.e. As and F^-) from waters, including reverse osmosis (RO),[1] nanofiltration (NF),[13] ion exchange,[1,14] electrocoagulation,[15,16] and adsorption.[1,2,17–28] Of these techniques, adsorption is the most cost-effective technique with high performance.[1,18,23,25]

Adsorption of As(V) or F^- from aqueous solution has been extensively studied over the last two decades with a focus on development of high-efficiency, low-cost and environmentally-benign adsorbents.[2,17–28] A wide variety of adsorbents were developed to remove As(V) and F^- from drinking water, e.g. Al-based adsorbents including activated alumina (AA),[1] aluminium hydroxide,[25] and mesoporous alumina[21] have been used to remove As(V) and F^- from aqueous solutions. Fe-based materials such as goethite,[19] goethite- and hematite-coated sand,[18] and granular ferric oxides (GFO)[18] have also been employed as adsorbents for aqueous

* *Correspondence to: F Li, Collaborative Innovation Center of Atmospheric Environment and Equipment Technology, Jiangsu Key Laboratory of Atmospheric Environment Monitoring and Pollution Control, School of Environmental Science and Engineering, Nanjing University of Information Science and Technology, 219 Ningliu Road, Nanjing 210044, China. E-mail: favorlee@gmail.com*

\# *Present address: School of Energy and Power Engineering, Xi'an Jiaotong University, Xi'an 710049, China.*

Collaborative Innovation Center of Atmospheric Environment and Equipment Technology, Jiangsu Key Laboratory of Atmospheric Environment Monitoring and Pollution Control, School of Environmental Science and Engineering, Nanjing University of Information Science and Technology, Nanjing, China

As(V) and F^-. Besides, bond char,[17,18] activated red mud[22] and industrial solid wastes[23] were observed to adsorb As(V) and F^- from wastewater. However, these adsorbents, especially Al- and Fe-based adsorbents, have a higher affinity for As(V) than F, leading to an undesired performance for simultaneous removal of both As(V) and F^-. In general, arsenic has a high affinity to metal (oxyhydr)oxides especially Al-, Fe-based (oxyhydr)oxides and titania,[21,25,29,30] whereas fluoride is likely to bind to solids containing rare earth elements.[2,26] Jing *et al.*[26] developed a novel TiO_2-La granular composite adsorbent that exhibited high adsorption capacities for As(III) (114 mg g^{-1}) and F^- (78.4 mg g^{-1}). Phillips *et al.*[27] compared the performance of two metal-loaded resin beads (i.e. Haix-Fe and Haix-Fe-Zr) in adsorptive removal of As(III/V) and F^- and concluded that Haix-Fe-Zr resin beads were more effective in removing F^- from the spiked groundwater compared with Haix-Zr resin beads. It would be, therefore, a good strategy to combine two or more functional groups (e.g. metal-based hydroxyls) into one composite adsorbent for simultaneous sequestration of both As(V) and F^-. However, there have been only a few attempts to investigate the co-uptake of both As(V) and F^- by adsorbents containing two components (e.g. Fe and Al,[20] Ti and lanthanum,[2,26] Fe and zirconium,[27] and Ti and cerium[31]), and no systematic studies to evaluate the effectiveness of other bimetallic composites for the co-uptake of As(V) and F^- have been reported yet.

Recently, it was shown that mesoporous alumina has an adsorption capacity as high as 450 mg g^{-1} for F^- while maintaining a superb As removal capacity meantime.[21] It has also demonstrated that introduction of mesoporosity into adsorbents can not only enhance the adsorption capacities for contaminants, but also accelerate the adsoption kinetics.[30,32–34] In this context, few works have been performed on the simultaneous removal of As(V) and F^- by mesoporous composite adsorbents, and the underlying mechanism at the molecular scale remains to be uncovered.

In this study, four mesoporous bimetallic oxides (MBOs) were prepared via the evaporation-induced self-assembly (EISA) method followed by calcination. The co-uptake characteristics and mechanisms of the MBOs for adsorptive removal of both As(V) and F^- were investigated using batch adsorption experiments, spectroscopy, and surface complexation modeling (SCM). Our study demonstrated the feasibility of simultaneous removal of As(V) and F^- by MBOs with higher adsorption affinity for As(V) and F^- compared with other bimetallic oxide composites. In addition, this work may also provide a strategy for contaminant-oriented high efficiency adsorbent development and deepen our understanding of the adsorption mechanisms of co-uptake of As(V) and F^- on dual-functional composite adsorbents.

MATERIALS AND METHODS

Chemicals

Pluronic P123 was obtained from Sigma-Aldrich Trading Co. Ltd (Shanghai, China). Iron(III) chloride ($FeCl_3$, ≥99%), aluminum isopropoxide ($C_9H_{21}AlO_3$, ≥98%, (Aladdin Chemical, Shanghai, China)), lanthanum nitrate hexahydrate ($La(NO_3)_3{\cdot}6H_2O$, 99%, Aladdin Chemical) and titanium tetrachloride ($TiCl_4$, ≥ 98%) were used as precursors for the synthesis of mesoporous bimetallic oxides (MBOs). Milli-Q ultrapure (18.2 MΩ-cm) water was used to prepare solutions.

Arsenate stock solution (1000 mg L^{-1}) was prepared by dissolving a specified amount of sodium arsenate dibasic heptahydrate ($Na_2HAsO_4{\cdot}7H_2O$, ≥ 98%, JT Baker Chemical, Phillipsburg, NJ, USA) with ultrapure water and stored in a refrigerator at 4 °C for further use. A given amount of sodium fluoride (NaF, ≥ 98%, Sinopharm Chemical, Shanghai, China) was dissolved in ultrapure water to yield fluoride stock solution (100 mg L^{-1}) that was also stored in a refrigerator for further use.

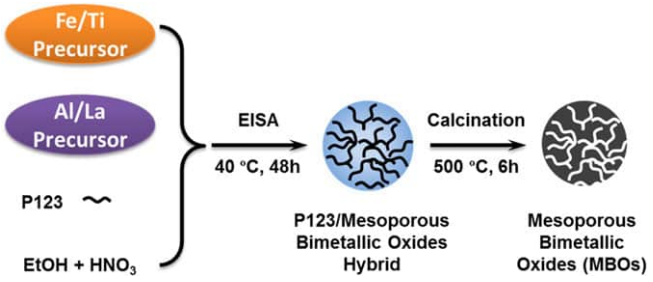

Scheme 1. Schematic illustration of preparation of MBOs via the EISA method followed by calcination.

Preparation of mesoporous bimetallic oxides (MBOs)

Four MBOs including mesoporous Fe/Al oxide, mesoporous Fe/La oxide, mesoporous Ti/Al oxide and mesoporous Ti/La oxide were prepared via the evaporation-induced self-assembly (EISA) method.[35] Briefly, in the case of preparation of mesoporous Fe/Al oxides, 2 g of P123 was dissolved in 40 mL of anhydrous ethanol (EtOH) under stirring until a homogeneous transparent solution was obtained. To this solution, 1.622 g (10 mmol) of $FeCl_3$ (Fe precursor) was added. After stirring for 0.5 h, 2.04 g (10 mmol) of $C_9H_{21}AlO_3$ (Al precursor) was introduced under stirring for 2 h and followed by addition of 1.6 mL of concentrated HNO_3 (67 wt.%). The mixture was stirred for 2–5 h prior to the EISA process in a 40 °C oven for 48 h. The dry solid sample was collected and calcinated at 500 °C in a tube furnace (ramp rate 1 °C min^{-1}) for 6 h and then recollected and stored for further use after cooling to room temperature. The synthetic mesoporous Fe/Al oxide was termed meso-Fe/Al. By replacing the Fe/Al precursors with other chemicals with the same dosages (in mmol), other MBOs were also prepared following the above procedures and termed meso-Fe/La, meso-Ti/Al, and meso-Ti/La, respectively (Scheme 1).

Characterization of MBOs

The crystallography information of MBOs was obtained using an X-ray diffraction (XRD) analyzer (XRD-6100, Shimadzu, Tokyo, Japan) at a tube voltage of 40 kV and a tube current of 30 mA using Cu-Kα radiation. The morphological structures were recorded on SU1510 (Hitachi, Japan) scanning electron microscope (SEM) at an accelerating voltage of 1.5 kV. The Brunauer–Emmett–Teller (BET) surface areas, pore volumes, and the Barrett–Joyner–Halenda (BJH) pore size distributions of MBOs were measured by N_2 adsorption–desorption at −196 °C using a gas adsorption analyzer (iQ-AG-MP, Quantachrome, Boynton Beach, FL, USA). Prior to the measurement, the samples were degassed at 105 °C for at least 12 h. Zeta (ζ) potential data were collected on a Zetasizer Nano ZS 90 apparatus (Malvern, Worcestershire, UK) using 10 mmol L^{-1} of $NaNO_3$ solution as background electrolyte. X-ray photoelectron spectroscope (XPS) (PHI 5000 Versa Probe, UIVAC-PHI, Japan) equipped with a monochromatized Al Kα X-ray source ($h\nu = 1486.6$ eV) and a hemispherical electron analyzer was employed to evaluate the surface properties of these samples. The C_{1s} peak (284.6 eV) was used for the calibration of binding energy values.

Batch adsorption experiments

Both adsorption envelope and isotherm experiments were performed at room temperature (*c.* 25 °C). In a typical adsorption envelope experiment, a set of suspensions containing 1 mg L^{-1} (or 30 mg L^{-1}) As(V), 10 mg L^{-1} F^-, and 2 g L^{-1} adsorbent (i.e., MBOs) were prepared in 15-mL capped polyethylene centrifuge tubes (Corning, Hartford, CT, USA). After adjusting to a desired pH over the range 3–12 with 0.1 mol L^{-1} NaOH and 0.1 mol L^{-1} HNO_3, the suspensions (10 mL) were bubbled with pure N_2 for 5 min to exclude dissolved CO_2 and then mixed on a Labquake tube rotator (Thermo Scientific, Waltham, MA, USA) for 24 h. The supernatant was collected by centrifugation (12 000 rpm for 15 min) and filtration with 0.45 μm PES filter (Navigator, Tianjin, China) for the measurement of As(V) and F^-. A background electrolyte of 10 mmol L^{-1} $NaNO_3$ was employed in the experiment.

Adsorption isotherm experiments were conducted in a background electrolyte (10 mmol L^{-1} $NaNO_3$) at pH 6.5 ± 0.2. The adsorbent dosage was fixed at 2 g L^{-1}, whereas the concentrations of As(V) and F^- were varied from 0.1–100 mg L^{-1} and 0.1–50 mg L^{-1}, respectively. The As(V) concentration was determined by hydride generation–atomic fluorescence spectrometry (HG-AFS, Skyray, AFS200, Kunshan, China). The F^- concentration was measured by ionic chromatography (ICS-2000, Dionex, Sunnyvale, CA, USA).[36] The solution pH values were measured on a Sartorius pH meter (PB-10) calibrated with standard pH 4.00, 7.00 and 10.01 buffers (Thermo, Waltham, MA, USA).

The competitive effects of co-anions including Cl^-, NO_3^-, SO_4^{2-}, CO_3^{2-}, and PO_4^{3-}, were also investigated individually following a well-defined method.[36] The initial concentration of these anions was set to the same as those of arsenate and fluoride anions (10 mmol L^{-1}), e.g., the molar ratio of As(V): F^-: Cl^- was 1:1:1 in the case of using Cl^- as a competitive anion. The competitive experiments were conducted individually at pH 6.5 ± 0.2 and 25 °C.

Surface complexation modeling

A charge distribution multi-site complexation (CD-MUSIC) model was employed to fit the adsorption envelopes of As(V) and F^- on meso-Fe/Al and meso-Ti/La. The 1-pK TPM adsorption option was used to calculate the reactions of As(V) and F^- with the adsorbents.

The non-protonated bidentate binuclear geometry (BB) was used for surface complex formation of As(V) with surface hydroxyl groups (i.e. ≡Fe-$OH^{-1/2}$ of meso-Fe/Al, ≡Ti-$OH^{+1/2}$ of meso-Ti/La), whereas a monodentate geometry was used for F^- adsorption by surface hydroxyl groups (i.e. ≡Al-$OH^{-1/2}$ of meso-Fe/Al, ≡La-$OH^{-1/2}$ of meso-Ti/La) in a ligand exchange manner.[2] The proton affinity constant ≡Fe-$OH^{-1/2}$ was set to 8.3 (pH_{PZC} of meso-Fe/Al), and the proton affinity constants ≡Al-$OH^{-1/2}$, ≡Ti-$OH^{+1/2}$ and ≡La-$OH^{-1/2}$ were obtained from previous references.[2,37] The CD values for different complexes were obtained from previous reports.[2,37,38] The adsorption constants of both As(V) and F^- were obtained by best fitting model-calculated values to the experiment data. The calculation was performed by using the chemical equilibrium program Visual MINTEQ 3.1 to simulate the adsorption and the aqueous reactions with a fixed ionic strength of 10 mmol L^{-1} $NaNO_3$. The surface parameter and species used in the CD-MUSIC modeling are summarized in Table S2.

RESULTS AND DISCUSSION

Properties of MBOs

The XRD patterns of MBOs are given in Fig. 1. It is obvious that the MBOs show a set of quite different reflections as their compositions varied from Fe-Al, Fe-La, Ti-Al to Ti-La. A group of well-defined peaks assignable to hematite (JCPDS #33-0664) was observed for meso-Fe/Al (red curve in Fig. 1), and no peaks corresponding to alumina were found, implying that all Al atoms have probably entered into the lattices of hematite and occupied the same spacial positions as Fe atoms. Two major phases La_2O_3 (JCPDS #05-0602, marked L_1) and $La_2O_2CO_3$ (JCPDS #37-0804, marked L_2) have been confirmed for meso-Fe/La (black curve in Fig. 1). The peaks at $2\theta = 10.7°$, 16.3°, 18.8°, 19.4° are probably derived from Fe-La complexes formed during the calcination process.[39] The XRD pattern of meso-Ti/Al showed some broad peaks attributed to anatase (JCPDS #21-1272) and no peaks of Al-containing phases were observed, suggesting that Al oxide was probably in amorphous forms (olive curve in Fig. 1). As indicated in Fig. 1 (blue curve), meso-Ti/La was a mixture of rutile (JCPDS #21-1276), La_2O_3 and $La_2O_2CO_3$, amorphous LaOOH and titania were also probably formed as evidenced by the broad reflection at $2\theta = 25–35°$ range.[2]

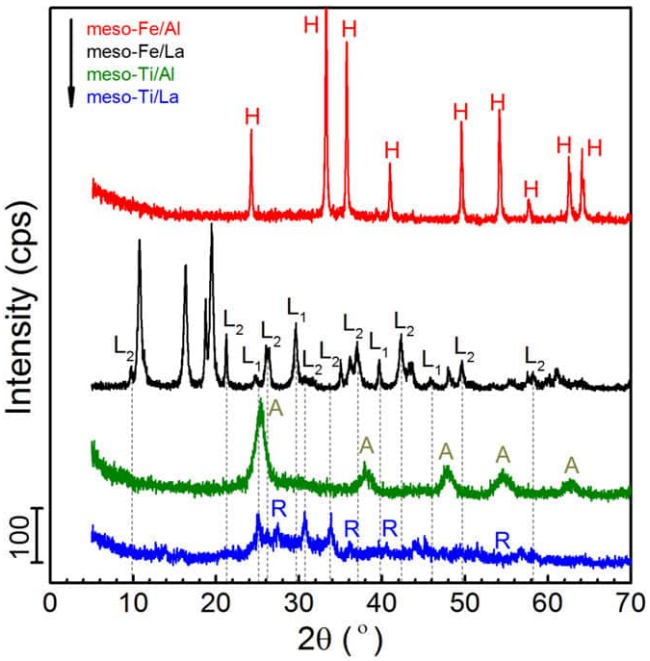

Figure 1. XRD patterns of synthetic mesoporous bimetallic oxides (MBOs). (A: anatase, H: hematite, L_1: La_2O_3, L_2: $La_2O_2CO_3$, R: rutile).

As shown in Fig. 2, irregular, coarse and aggregated nanoparticles were observed for meso-Fe/Al, meso-Fe/La, and meso-Ti/La (Fig. 2 (A, B and D)). Well-defined hexagonal anatase crystals were also observed for meso-Ti/Al (Fig. 2(C)). The particle size distributions (PSDs) were also analyzed with ImageJ (version 1.51), shown as the insets in Fig. 2. The mean particle sizes were 18, 21, 31, and 4 μm for meso-Fe/Al, meso-Fe/La, meso-Ti/Al, and meso-Ti/La, respectively. Figure 3 depicts the N_2 adsorption–desorption isotherms and corresponding pore size distributions. The pore size distributions were calculated with the BJH method using the desorption data of the isotherms. It is obvious that they can be classified as type II isotherms (IUPAC classification) with hysteresis loops of type H3, which indicates that the porous structures of all MBOs were derived from the mesopores (or macropores) that are formed by non-rigid aggregates of nanoparticles. This observation confirms the above SEM analysis (Fig. 2). The pore size distributions were fairly narrow with mean pore diameter values

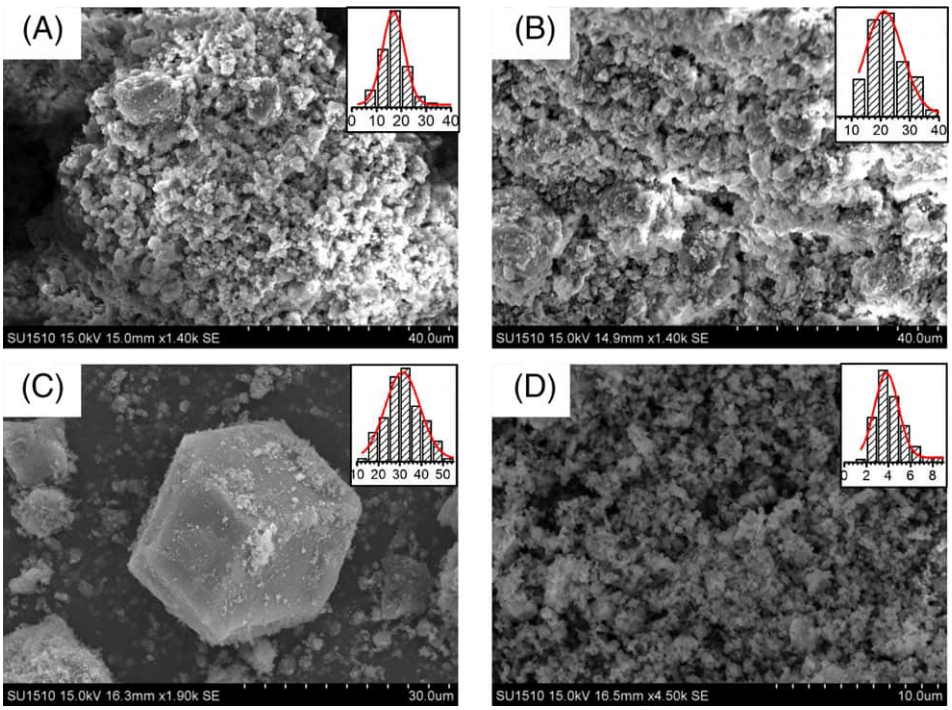

Figure 2. SEM images of (A) meso-Fe/Al, (B) meso-Fe/La, (C) meso-Ti/Al, (D) meso-Ti/La. The insets are the corresponding particle size distributions (unit: μm) of MBOs.

of 4.9, 5.6, and 3.9 nm for meso-Fe/Al, meso-Ti/Al, and meso-Ti/La, respectively (insets of Fig. 3(A, C, D)), suggesting that the pores are uniform and well-defined mesopores. However, meso-Fe/La shows a broad pore size distribution (inset of Fig. 3(B)), indicating that meso-Fe/La is of hierarchical structure containing both macropores and mesopores. The BET specific surface areas are 83, 13, 200, and 55 m^2 g^{-1} for meso-Fe/Al, meso-Fe/La, meso-Ti/Al, and meso-Ti/La, respectively, less than those previously reported for mesoporous metal oxides.[35] This observation was likely due to the properties and compatibilities of the precursors of these MBOs, which in turn results in the collapse of the mesopores and the dense aggregates upon calcination.

Point of zero charge

Figure 4 presents zeta potential versus solution pH values obtained for MBOs in the presence of a background electrolyte of 10 mmol L^{-1} $NaNO_3$ and/or additional 1 mmol L^{-1} NaF or Na_2HAsO_4. The point of zero charge (pH_{PZC}) of meso-Fe/Al occurred at pH 8.3 (Table S1), consistent with previous report data.[40] The presence of 1 mmol L^{-1} NaF shifted the pH_{PZC} value of meso-Fe/Al from pH 8.3 to ~ 8.1, whereas the occurrence of 1 mmol L^{-1} Na_2HAsO_4 shifted the PZC from pH 8.3 to pH ~ 7.9 (Fig. 4(A)). These phenomena are indirect macroscopic evidence of inner-sphere surface complex formation of both F^- and As(V) on meso-Fe/Al.[41] The pH_{PZC} value of meso-Fe/La was found to occur at pH 8.2 (Fig. 4(B)), and shifted to pH 9.3 with the appearance of 0.1 mmol L^{-1} F^- and shifted to pH 7.8 in the co-occurrence of 0.1 mmol L^{-1} As(V), suggesting that $F^-$was likely to form outer-sphere surface complexes while As(V) was bound as inner-sphere surface complexes on meso-Fe/La. The pH_{PZC} values of meso-Ti/Al and meso-Ti/La occurred at pH 8.9 and 7.8, respectively (Fig. 4(C, D)). They shifted to lower pH values in the presence of 0.1 mmol L^{-1} F^- or As(V), indicating that the formation of inner-sphere surface complexes of either F^- or As(V) took place. The shift in pH_{PZC} for As(V) adsorption ($pH_{PZC\text{-}As(V)}$ = 7.1) was greater than that for F^- adsorption ($pH_{PZC\text{-}F}$ = 7.3) on meso-Ti/Al, implying stronger adsorption for As(V) on meso-Ti/Al.

Adsorption envelopes

Two As(V) concentrations (1 mg L^{-1} and 30 mg L^{-1}) and one F^- concentration (10 mg L^{-1}) were used to study As(V) and F^- adsorption on MBOs over a pH range of 4–12 as suggested in reference.[26] Single- and dual-adsorbate systems were adopted and the adsorption envelopes are indicated in Fig. 5 for Fe-based MBOs and Fig. S1 (Supporting information) for Ti-based MBOs. Generally, the adsorption process is governed primarily by the point of zero charge of adsorbents. As shown in Fig. 5(A), on meso-Fe/Al, As(V) adsorption exhibited pH-independence at pH < 8.3 (pH_{PZC} of meso-Fe/Al, Table S1) for either low initial As(V) concentration (1 mg L^{-1}) or high initial As(V) concentration (30 mg L^{-1}). For the low initial As(V) concentration case, the pH-independent trend of As(V) adsorption can expand even to pH ~ 9, which is the pH_{PZC} value for meso-Fe/Al in the presence of 1 mmol L^{-1} As(V) and 10 mmol L^{-1} background electrolyte (Table S1). Both As(V) and F^- are negatively charged in these pH range, suggesting that pH_{PZC} controls As(V) adsorption on meso-Fe/Al. At pH above pH_{PZC}, the As(V) adsorption efficiency decreased with increasing pH values due to the electrostatic repulsion between the negatively charged surface of meso-Fe/Al and the negatively charged As(V). Moreover, also note that the presence of 10 mg L^{-1} fluoride ions has no influence on As(V) adsorption on meso-Fe/Al, implying that As(V) has a higher surface affinity than F^- to meso-Fe/Al. On meso-Fe/Al (Fig. 5(B)), F^- adsorption exhibited an increase in pH 4–6.0 to a narrow maximum in pH 6.0–7.5 and then decreased gradually with increasing solution pH due to electrostatic repulsion and a possible competitive adsorption of hydroxide ions. Similar pH-dependent, adsorption behavior has been observed previously for F^- adsorption on amorphous Al hydroxides.[25] It is obvious that the presence of 1 mg L^{-1} of As(V) as a co-adsorbate

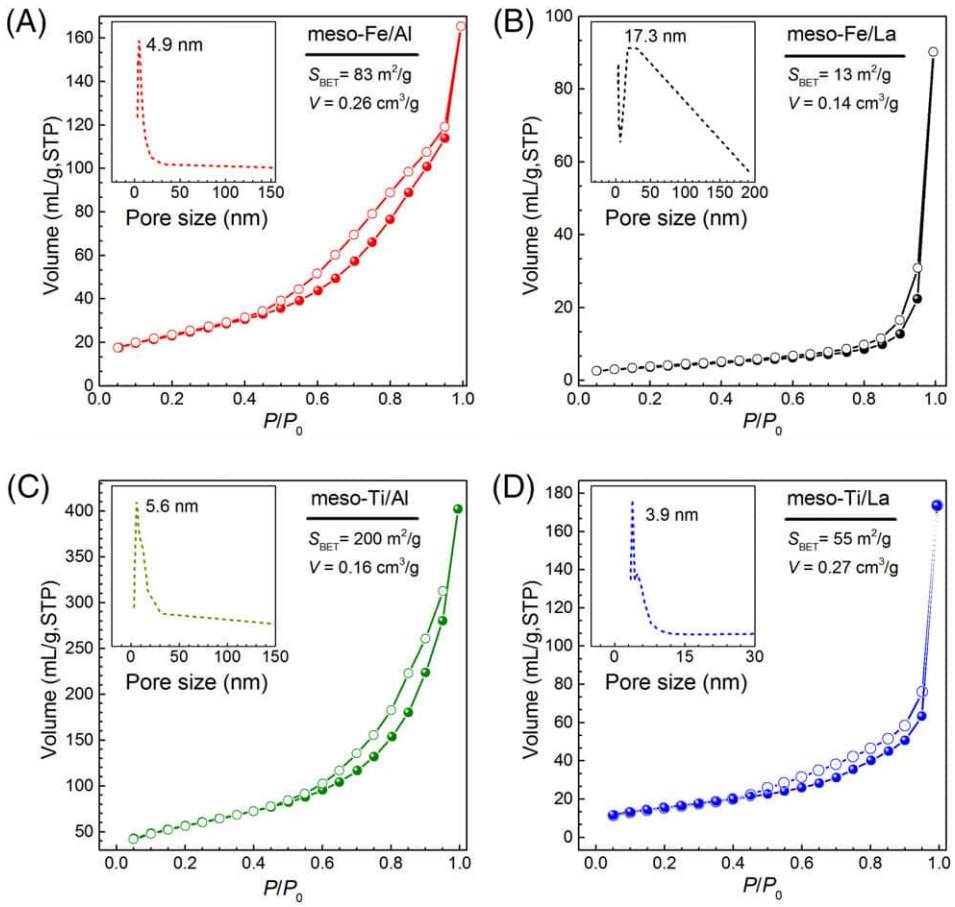

Figure 3. N_2 adsorption–desorption isotherms and BJH pore size distributions (insets) of (A) meso-Fe/Al, (B) meso-Fe/La, (C) meso-Ti/Al, (D) meso-Ti/La.

will slightly decrease F^- adsorption at pH < 7.5 probably due to the competition from As(V) for the binding sites (surface hydroxyls, ≡Me-OH), while the presence of 30 mg L^{-1} As(V) will promote F^- adsorption slightly at pH > 7 (Fig. 5(B)). This is possible due to the lower electrostatic repulsion of F^- than As(V) and the more binding sites left due to the rapid decrease in As(V) adsorption at pH > 8 (Fig. 5(A)).

On meso-Fe/La, both As(V) and F^- adsorption displayed similar behaviors to those of meso-Fe/Al (Fig. 5(C, D)). Nevertheless, the competitive effect of As(V) on F^- adsorption was more obvious compared with meso-Fe/Al (Fig. 5(D)). A similar observation was also reported in a previous study of F^- adsorption on red mud.[22] On Ti-based MBOs (i.e. meso-Ti/Al and meso-Ti/La), both As(V) and F^- adsorption exhibited analogous trends to Fe-based MBOs (Fig. S1). Our results suggest that, (i) both As(V) and F^- adsorption on the four MBOs are pH-dependent in the pH range studied (i.e., pH 4–12); (ii) As(V) shows a higher surface affinity than F^- on MBOs; and (iii) As(V) can compete with F^- for the binding sites effectively, while F^- has little influence on As(V) adsorption on MBOs.

Adsorption isotherms

Adsorption isotherm experiments were performed at 15 °C and 30 °C respectively to investigate the influence of experimental temperature (*T*) on adsorption capacity of MBOs. As shown in Figs 6 and 7, the adsorption capacities increased with increasing initial As(V) and F^- anion concentrations and reached a plateau, which represents the maximum adsorption capacity of the MBOs. This increase in adsorption capacities of MBOs is derived from the higher driving force for mass transfer at higher initial As(V) and F^- concentrations. The experimental data were fitted by both Langmuir and Freundlich isotherm models as follows:

$$Q_e = \frac{Q_m k_L C_e}{1 + k_L C_e} \quad (1)$$

$$Q_e = k_F C_e^{1/n} \quad (2)$$

where C_e is equilibrium concentration (mg L^{-1}), Q_e is the adsorption capacity (mg g^{-1}), Q_m is the theoretical maximum adsorption capacity (mg g^{-1}), and k_L (L mg^{-1}) is the Langmuir constant related to free energy of adsorption, k_F (L g^{-1}) and *n* are empirical constants associated with the Freundlich model. The fitting parameters of both Langmuir and Freunlich model are calculated by Origin 9.0 (OriginLab Co, Northampton, MA, USA) and tabulated in Tables 1 and 2, respectively. The high correlation coefficients (R^2) of both Langmuir and Freunlich models indicate than both algorithms can well fit the experimental data.

Temperature has a different influence on As(V) and F^- adsorption on different MBOs. For example, the As(V) adsorption capacities (Q_{As}) of meso-Fe/Al and meso-Ti/La decreased with increasing temperature, while the Q_{As} values of meso-Fe/La and meso-Ti/Al increased notably as temperature was increased from 15 °C to 30 °C (Fig. 6 and Table 1). However, F^- adsorption onto MBOs exhibited a different trend as temperature was varied. The F^- adsorption capacities (Q_F) of Fe-based MBOs (i.e. meso-Fe/Al

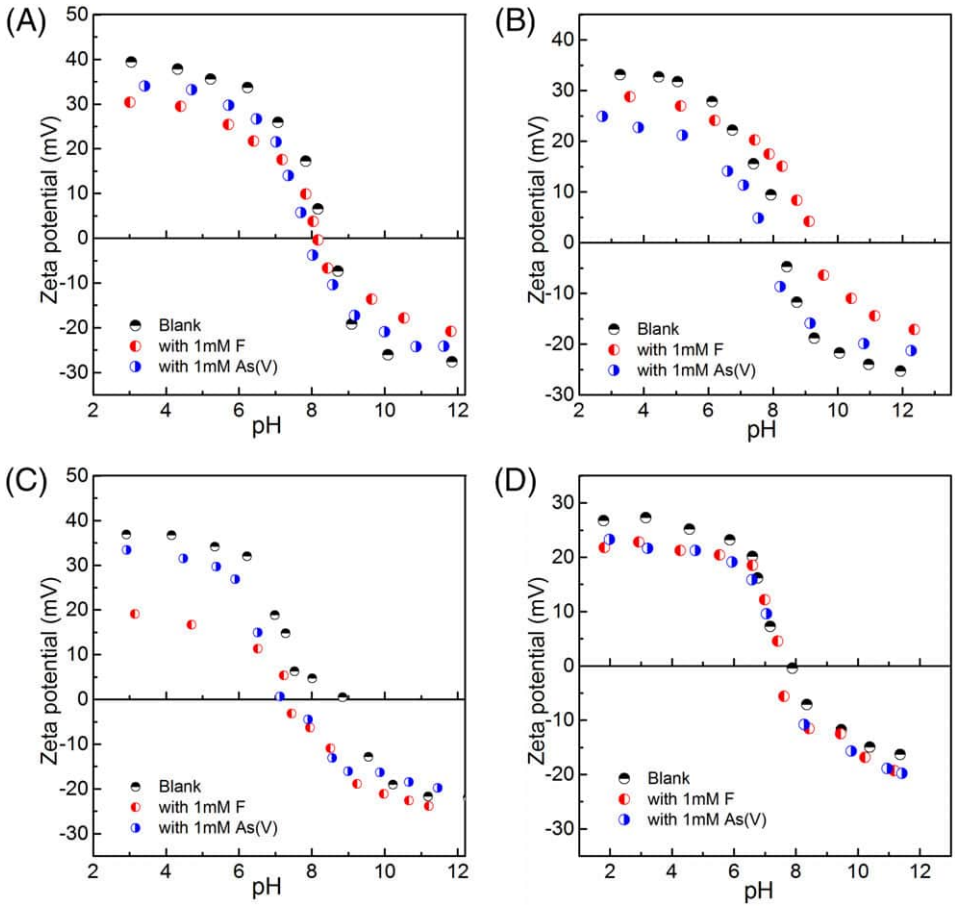

Figure 4. Zeta potential profiles of (A) meso-Fe/Al, (B) meso-Fe/La, (C) meso-Ti/Al, (D) meso-Ti/La (ionic strength: 10 mmol L^{-1} $NaNO_3$, [adsorbent]: 0.1 g L^{-1}, 20 °C).

and meso-Fe/La) increased with increasing temperature, whereas the Q_F values of Ti-based MBOs (i.e., meso-Ti/Al and meso-Ti/La) declined as temperature was increased. Generally, the higher adsorption capacity at higher temperature indicates that adsorption is an endothermic process, otherwise the adsorption is exothermic. The isotherm data suggested that As(V) adsorption on meso-Fe/Al and meso-Ti/La was exothermic, while As(V) adsorption on meso-Fe/La and meso-Ti/Al was endothermic. Likewise, F^- adsorption was endothermic for Fe-based MBOs but exothermic for Ti-based MBOs. Previous data have shown that As(V) and F^- adsorption on metal oxides can be either endothermic or exothermic depending on the experimental conditions and the properties of adsorbents and adsorbates.[31,40,42,43] It was also found that the coexistence of As(V) and F^- in solutions played a crucial role in both Q_{As} and Q_F values of MBOs. Compared with the cases of single As(V) adsorption by MBOs, the presence of F^- in As(V) adsorption slurries enhanced As(V) adsorption onto Fe-based MBOs but depressed As(V) adsorption onto Ti-based MBOs (Fig. 6). The maximum As(V) adsorption capacities ($Q_{m\text{-}As}$) of meso-Ti/Al and meso-Ti/La at 15 °C decreased respectively from 27.12 mg g^{-1} to 17.67 mg g^{-1} (a reduction of 35%), and from 81.42 mg g^{-1} to 20.98 mg g^{-1} (a reduction of 74%) (Table 1). This implies that F^- ions compete with As(V) for the adsorption sites (≡Me-OH) of meso-Ti/Al and meso-Ti/La, and that the mechanisms for As(V) and F^- adsorption on Fe-based MBOs, i.e., meso-Fe/Al and meso-Fe/La, are totally different. Likewise, the coexistence of As(V) in F^- adsorption slurries improved the Q_F of meso-Fe/La slightly but remarkably reduced the Q_F of meso-Fe/Al, meso-Ti/Al and meso-Ti/La (Fig. 7). As shown in Table 1, the maximum F^- adsorption capacities ($Q_{m\text{-}F}$) of meso-Fe/Al, meso-Ti/Al and meso-Ti/La at 15 °C reduced respectively from 18.64 mg g^{-1} to 14.54 mg g^{-1} (a reduction of 22%), from 28.20 mg g^{-1} to 17.14 mg g^{-1} (a reduction of 39%), and from 44.37 mg g^{-1} to 12.99 mg g^{-1} (a reduction of 71%). Comparison of the reduction in As(V) and F adsorption capacities on MBOs suggested that As(V) had a higher affinity than F^- to Fe-based MBOs, and that Ti-based MBOs exhibited a similar affinity towards As(V) and F^- (Table 1). This observation is consistent with the above adsorption envelope results.

The $Q_{m\text{-}As}$ values of meso-Fe/Al, meso-Ti/Al, and meso-Ti/La at 15 °C were 33.35 mg g^{-1}, 27.12 mg g^{-1}, and 81.42 mg g^{-1} respectively (Table 1), and the $Q_{m\text{-}F}$ values of meso-Ti/Al and meso-Ti/La were 28.2 mg g^{-1} and 44.37 mg g^{-1} respectively. These Q_m values place MBOs among the top adsorbents for As(V) and F^- uptake (Table 3). The relatively high surface areas, mesoporous structures of MBOs enable most of their binding sites to be available and accessible for As(V) and F^-, improving their adsorption efficiency for co-uptake of As(V) and F from aqueous solutions.

To study the recycling performance of MBOs, meso-Fe/Al and meso-Fe/La were selected as candidates for desorption–adsorption tests. Typically, after adsorption in a mixture (10 mg L^{-1} As(V) + 10 mg L^{-1} F^-, pH = 6.5 ± 0.2), the exhausted meso-Fe/Al (20 mg) was regenerated with 5 mL of dilute NaOH (0.1 mol L^{-1}) three times, followed by rinsing with

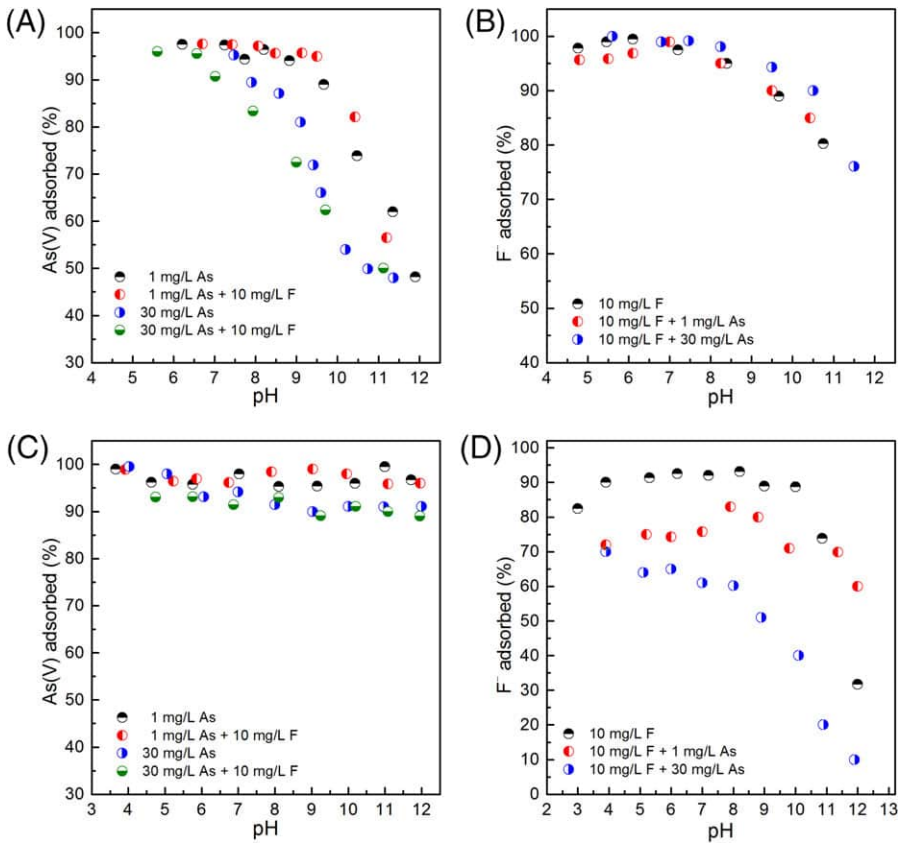

Figure 5. Effect of solution pH on As(V) and F^- adsorption on meso-Fe/Al (A, B) and meso-Fe/La (C, D).

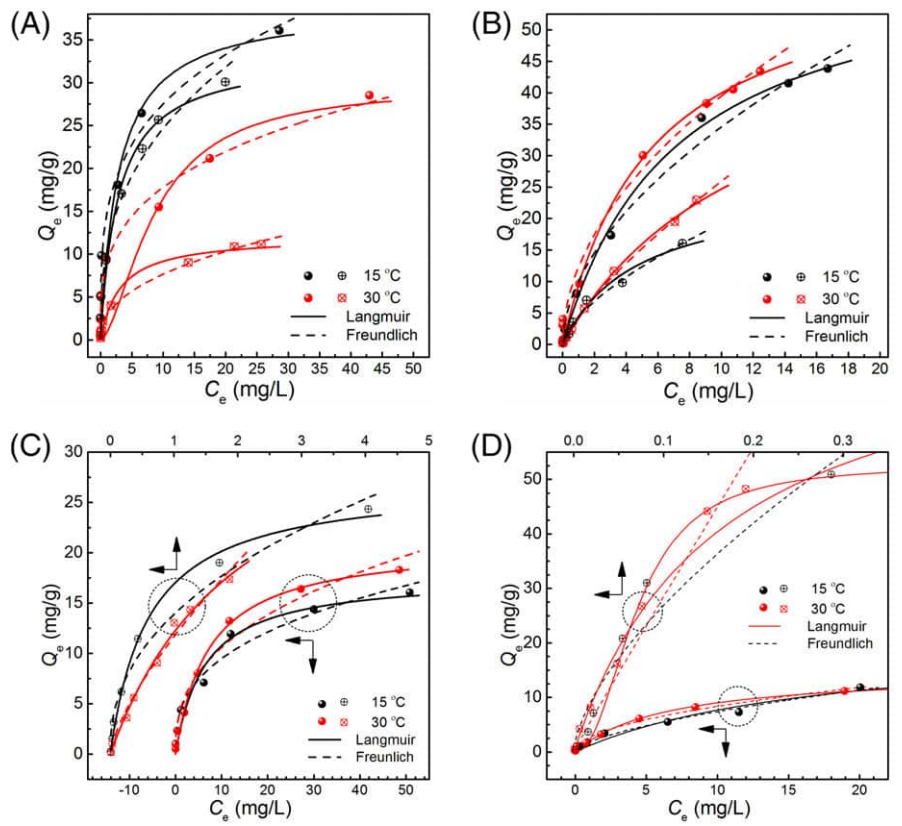

Figure 6. Adsorption isotherms of As(V) on (A) meso-Fe/Al, (B) meso-Fe/La, (C) meso-Ti/Al, (D) meso-Ti/La in 10 mmol L^{-1} $NaNO_3$ solution at pH = 6.5 ± 0.2. Note: cross and solid circles refer to the single-adsorbate (As) system and the dual-adsorbate (As + F) system, respectively.

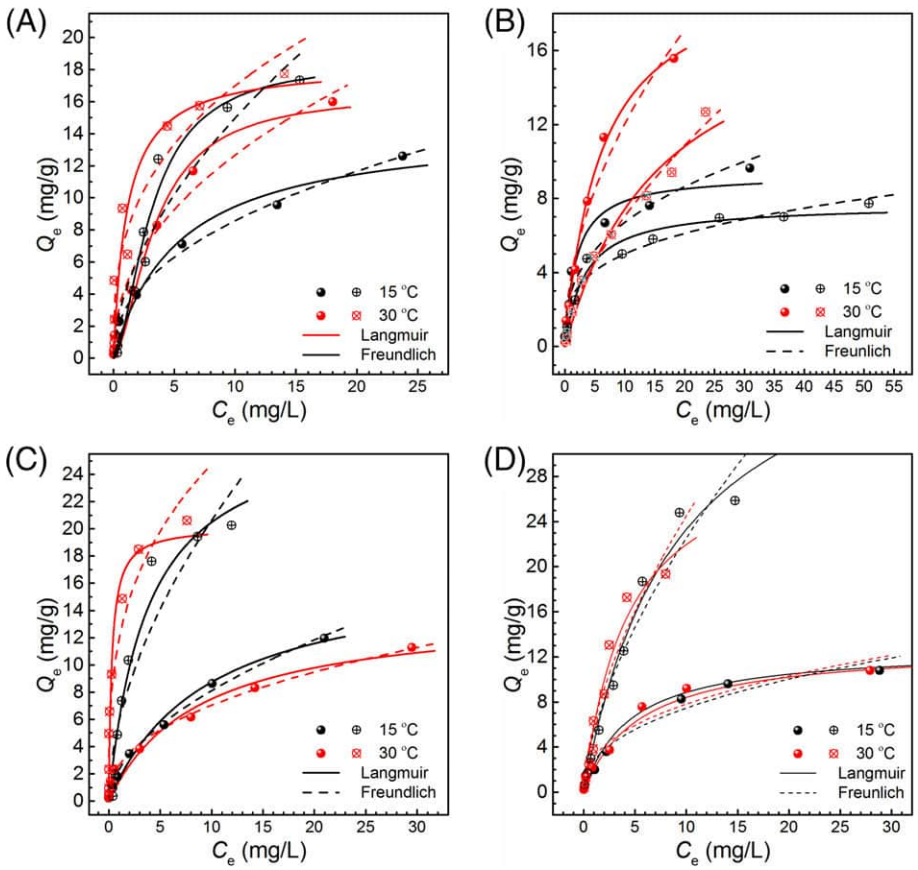

Figure 7. Adsorption isotherms of F on (A) meso-Fe/Al, (B) meso-Fe/La, (C) meso-Ti/Al, (D) meso-Ti/La in 10 mmol L^{-1} $NaNO_3$ solution at pH = 6.5 ± 0.2. Note: cross and solid circles refer to the single-adsorbate (F) systems and the dual-adsorbate (As + F) systems, respectively.

Table 1. Langmuir parameters for As and F adsorption on MBOs

			15 °C			30 °C		
Adsorbent	Target adsorbate	Solution	Q_m (mg g^{-1})	K_L (L mg^{-1})	R^2	Q_m (mg g^{-1})	K_L (L mg^{-1})	R^2
Meso-Fe/Al	As(V)	As	33.35	0.351	0.971	12.07	0.315	0.988
		As + F	38.98	0.344	0.912	29.65	0.029	0.925
	F	F	18.64	0.147	0.964	18.35	0.090	0.907
		As + F	14.54	0.186	0.972	16.57	0.134	0.959
Meso-Fe/La	As(V)	As	25.27	0.210	0.982	54.48	0.083	0.998
		As + F	62.70	0.141	0.996	62.10	0.180	0.988
	F	F	7.67	0.304	0.962	19.82	0.059	0.972
		As + F	9.30	0.542	0.971	20.90	0.166	0.994
Meso-Ti/Al	As(V)	As	27.12	1.655	0.994	38.12	0.465	0.992
		As + F	17.67	0.156	0.965	20.97	0.137	0.993
	F	F	28.20	0.265	0.948	20.19	3.387	0.944
		As + F	17.14	0.104	0.987	14.08	0.114	0.949
Meso-Ti/La	As(V)	As	81.42	6.144	0.935	52.68	0.495	0.972
		As + F	20.98	0.058	0.961	14.81	0.155	0.991
	F	F	44.37	0.110	0.981	31.47	0.231	0.964
		As + F	12.99	0.183	0.987	12.80	0.224	0.984

20 mL of ultrapure water before the next adsorption cycle. The desorption–adsorption experiments were performed at 25 °C for five successive cycles and the results are depicted in Fig. S2 (Supporting information). It is obvious that the adsorption efficiencies of both As(V) and F^- decreased as the cycle number increased. As(V) adsorption efficiencies of meso-Fe/La and meso-Fe/Al decreased from ~ 88% and ~ 85% to ~ 60% and 52%, respectively. F^- adsorption efficiencies of meso-Fe/La and meso-Fe/Al declined from ~ 72% and ~ 93% to ~ 44% and ~ 60%, respectively. The loss in adsorption efficiencies of both As(V) and F^- is probably due

Table 2. Freundlich parameters for As(V) and F adsorption on MBOs

Adsorbent	Target adsorbate	Solution	15 °C			30 °C		
			K_F	1/*n*	R^2	K_F	1/*n*	R^2
Meso-Fe/Al	As(V)	As	10.52	0.369	0.984	2.82	0.432	0.992
		As + F	14.65	0.274	0.983	8.82	0.304	0.981
	F	F	4.17	0.555	0.896	7.60	0.350	0.912
		As + F	3.08	0.445	0/996	4.47	0.453	0.984
Meso-Fe/La	As(V)	As	4.41	0.639	0.984	4.48	0.762	0.998
		As + F	10.01	0.538	0.990	12.28	0.507	0.987
	F	F	2.56	0.290	0,949	1.65	0.628	0.988
		As + F	2.91	0.363	0.946	3.72	0.509	0.973
Meso-Ti/Al	As(V)	As	13.89	0.434	0.972	11.67	0.711	0.984
		As + F	4.21	0.353	0.976	4.34	0.387	0.969
	F	F	5.81	0.550	0.872	11.82	0.321	0.908
		As + F	2.31	0.545	0.995	2.62	0.430	0.996
Meso-Ti/La	As(V)	As	118.52	0.645	0.894	267.40	0.973	0.960
		As + F	1.79	0.618	0.987	2.66	0.497	0.988
	F	F	5.34	0.625	0.951	6.02	0.609	0.922
		As + F	2.80	0.425	0.967	3.11	0.400	0.938

Table 3. Comparison of the maximum As(V) and F adsorption capacities of MBOs with other published data

Adsorbents	Experimental conditions	Q_m (mg g^{-1})		Reference
		As(V)	F	
Activated red mud	pH = 7.0, *T* = 25 °C	5.16	3.96	[22]
Ce-Ti oxide adsorbent	pH = 6.5, *T* = 25 °C	7.5	–	[31]
β-$Al(OH)_3$	pH = 6.0, *T* = 25 °C	14.29	–	[47]
Nickel/nickel boride nanoparticles	pH = 7.0, *T* = 20 °C	23.4	–	[4]
Ti and La oxides loaded activated carbon (TLAC)	pH = 7.0, *T* = 20 °C	30.3	27.8	[2]
Fe-Al mixed oxide	pH = 6.9, *T* = 20 °C	–	12.0	[40]
Fe-Al-Ce trimetal oxide	pH = 7.0, *T* = 25 °C	–	12.2	[48]
Al-Ce hybrid adsorbent	pH = 6.0, *T* = 20 °C	–	27.5	[49]
Meso-Fe/Al	pH = 6.5, *T* = 15 °C	33.35	18.64	This study
Meso-Ti/Al	pH = 6.5, *T* = 15 °C	27.12	28.20	This study
Meso-Ti/La	pH = 6.5, *T* = 15 °C	81.42	44.37	This study

to the loss of adsorption sites during the regeneration process. Nevertheless, these two MBOs with such recycling performance are expected to be practically used as alternative adsorbents for simultaneous removal of As(V) and F^- from aqueous solution.

Effect of competitive anions

There are also other naturally occurring anions in As(V) and F^- contaminated water,[2–4] which may compete with both As(V) and F^- for the adsorption sites. Herein, the effect of competitive anions such as Cl^-, NO_3^-, SO_4^{2-}, CO_3^{2-}, and PO_4^{3-} on the adsorption of As(V) and F^- was studied individually at pH 6.5 ± 0.2 and 25 °C with a molar ratio of 1 (As(V)): 1 (F^-): 1 (competitive anion). As shown in Fig. 8, the adsorption efficiencies of As(V) by both meso-Fe/Al and meso-Fe/La were hindered by PO_4^{3-} compared with Cl^-, NO_3^-, SO_4^{2-}, and CO_3^{2-}. Besides, the adsorption efficiencies of F^- by both MBOs were impeded by PO_4^{3-} and SO_4^{2-} compared with other anions tested. Similar effects of phosphate and sulfate on metal oxide adsorbents for removal of As(V) and F^- were also observed previously.[2,14,19] In addition, the suppressive effect of these competitive anions was more noteworthy for F^- than for As(V), implying As(V) has a higher affinity to these MBOs than F^-.[2]

XPS analysis

XPS analysis has been widely employed to study the interaction between As(V) and/or F^- and adsorbents at the water/adsorbent interface.[14,21,24,26,43,44] The XPS spectra of MBOs was recorded before and after adsorption of As(V) and F^-, and the results are shown in Fig. 9 and Figs S3 – S5 (Supporting information). As shown in Fig. 9(A), besides the peaks of Fe 2*p*, O 1*s*, C 1*s*, Al 2*s*, Fe 3*s* and Al 2*p* being observed in both fresh and spent meso-Fe/Al (i.e. before and after adsorption), four peaks at binding energies about 684.5 eV, 227.1 eV, 142.5 eV and 42.7 eV were also observed for the spent meso-Fe/Al. These peaks can be assigned to F 1*s*, As 3*s*, As 3*p*, and As 3*d*, respectively. Likewise, XPS peaks corresponding to F 1*s*, As 3*s*, As 3*p*, and As 3*d*, respectively, were also observed for spent meso-Fe/La, meso-Ti/Al, and meso-Ti/La (see Figures S3A – S5A in Supporting information). This observation indicates that both As(V) and F^- had been adsorbed to the surface of MBOs, in agreement with the above batch adsorption results.

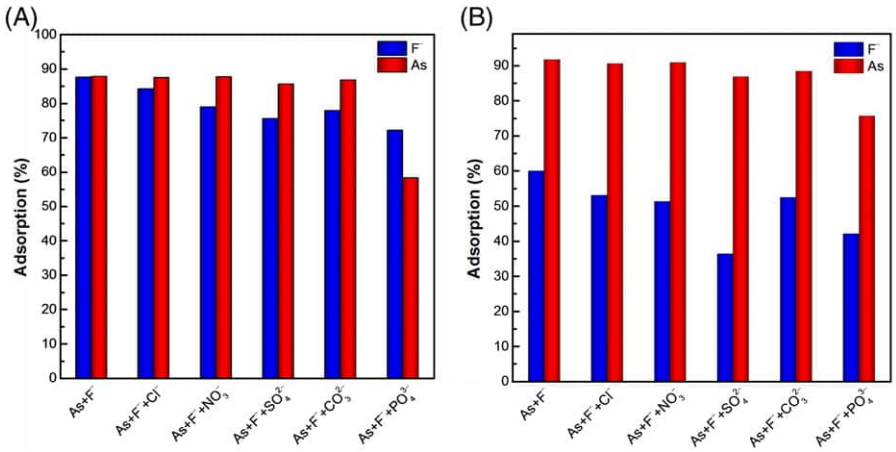

Figure 8. Effects of competitive anions ([As(V)]:[F^-]:[competitive anion] = 1:1:1) on As(V) and F^- adsorption onto (A) meso-Fe/Al and (B) meso-Fe/La at pH = 6.5 ± 0.2.

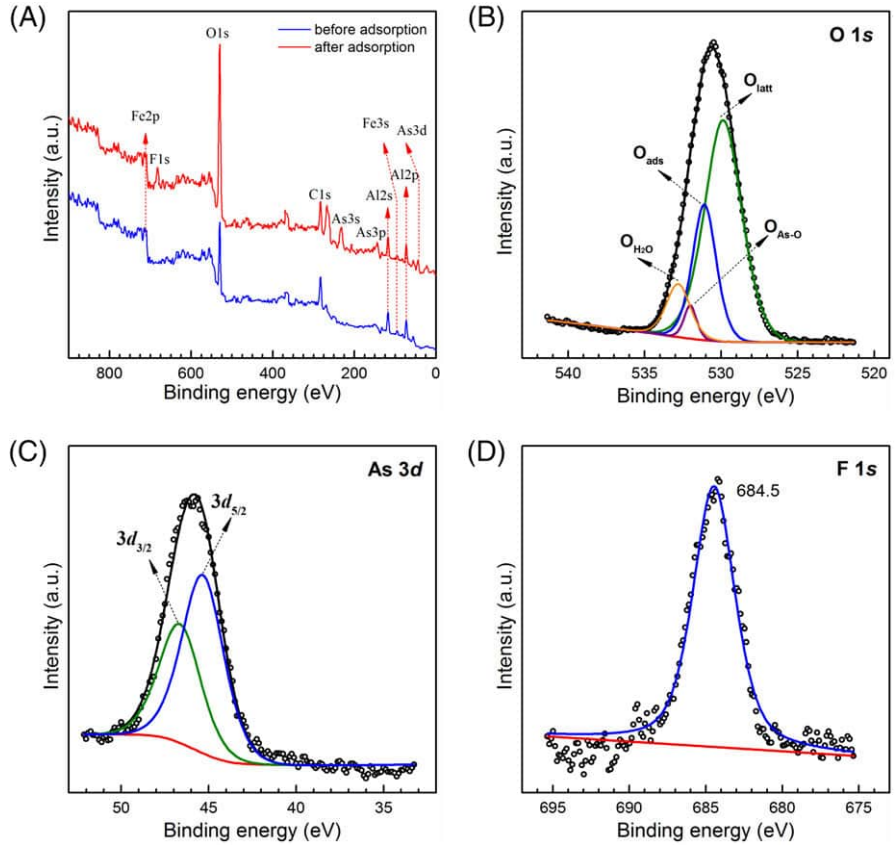

Figure 9. XPS spectra of meso-Fe/Al: (A) survey scans of fresh and spent adsorbent; high-resolution scans of (B) O 1*s*, (C) As 3*d*, (D) F 1*s* of spent adsorbent.

The high-resolution scan of O 1*s* peak of spent meso-Fe/Al can be deconvoluted into four different components at binding energies of 529.9 eV, 531.1 eV, 532.0 eV, and 532.8 eV, respectively (Fig. 9(B) and Table S3). The peaks at 529.9 eV, 531.1 eV, and 532.8 eV can be assigned to the lattice metal–oxygen bond (denoted as O_{latt}), surface hydroxyls bond (denoted as O_{ads}), and adsorbed water hydroxyl bond (termed as O_{H2O}), respectively.[26,44] The peak at 532.0 eV is attributed to As–O bonds (denoted as $O_{As\text{-}O}$) (Fig. 9(B)). For other spent MBOs, the high-resolution scans of O 1*s* peak can also be deconvoluted into four components attributable to O_{latt}, O_{ads}, O_{H2O}, and $O_{As\text{-}O}$ bonds respectively (see Figures S3B – S5B and Table S3), implying the uptake of As(V) on MBOs. Furthermore, it was also noted that the intensity of O 1*s* peak increased obviously after adsorption of As(V) and F^- (c.f. Fig. 9(A) and Figs S3A – S5A), suggesting that surface hydroxyls are likely to associate with both As(V) and F^- adsorption on these MBOs. Note that the high-resolution scans of As 3*d* and F 1*s* peaks of the spent meso-Fe/Al appeared at binding energies 45.8 eV and 684.5 eV, respectively (Fig. 9(C, D)), which can be assigned to As(V) and F^-.[14,21,44] Similar observations were made in the high-resolution scans of As 3*d* and F 1*s* peaks of other MBOs (see Figures S3–S5). This implies that the chemical valences of both As(V) and F^- remain unchanged after the adsorption.

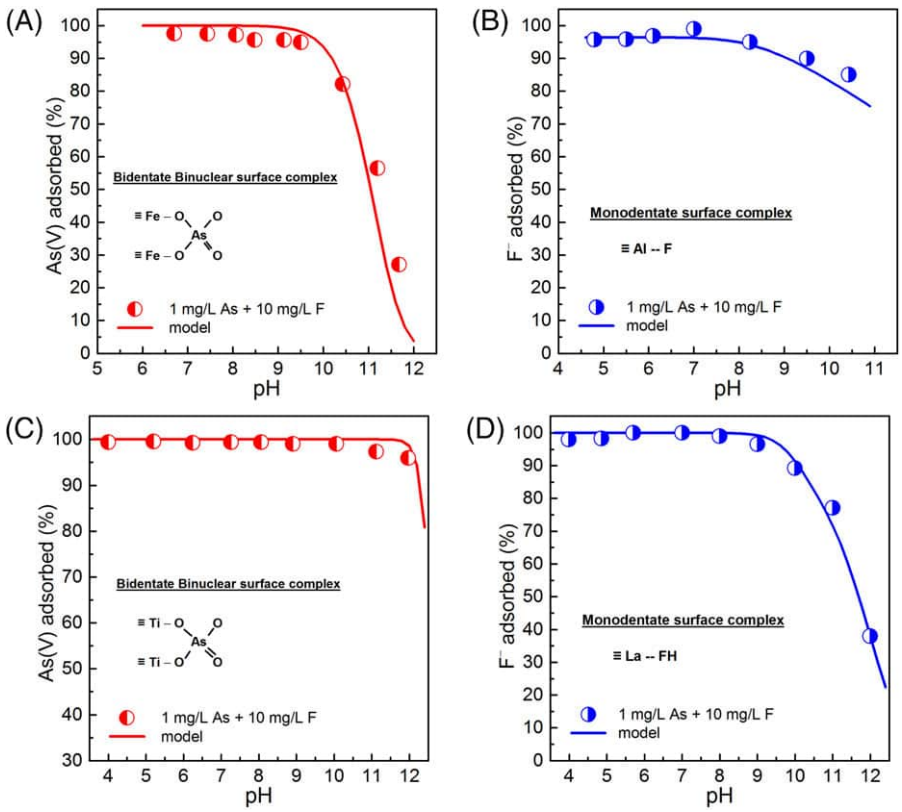

Figure 10. Experimental (symbols) and CD-MUSIC modeling (lines) of As(V) and F^- on (A, B) meso-Fe/Al and (C, D) meso-Ti/La in 0.01 mol L^{-1} $NaNO_3$ solutions. (As(V) = 1 mg L^{-1}, F^- = 10 mg L^{-1}, adsorbent dose = 2 g L^{-1}).

SCM modeling and adsorption mechanism

Due to the limited adsorption constants available in the literature, only meso-Fe/Al and meso-Ti/La were chosen to simulate the adsorption envelopes of a dual-adsorbate system (1 mg L^{-1} As(V) + 10 mg L^{-1} F^-) in 0.01 mol L^{-1} $NaNO_3$. The model assumed that As(V) was adsorbed by ≡Fe-$OH^{-1/2}$ and ≡Ti-$OH^{+1/2}$ groups, and F^- was bound to ≡Al-$OH^{-1/2}$ and ≡La-$OH^{-1/2}$ groups.[2] It should be noted that although Al-containing oxides were not detected by XRD (Fig. 1), XPS analysis verified the existence of surface Al atoms on meso-Fe/Al (Fig. 9(A)), which means that the above model assumption is sensible. It had shown that As(V) was adsorbed via two bidentate geometries.[45] On the other hand, ≡Al-$OH^{-1/2}$ was generally considered as an active site for binding As(V),[37,46] our fitting result of an initial modeling attempt by introduction of a second bidentate surface complex ($\equiv(AlO)_2AsO_2$) always overestimated the adsorption envelope at the high pH range. Therefore, we modeled our data by using only $\equiv(FeO)_2AsO_2$, $\equiv(TiO)_2AsO_2$, ≡AlF and ≡LaFH surface species. The reactions can be formulated as follows:

$$2 \equiv Fe - OH^{-1/2} + AsO_4^{3-}(aq) + 2H^+(aq) \leftrightarrow \equiv Fe_2O_2^{1.47} AsO_2^{-1.47} + 2H_2O(l) \quad (3)$$

$$\equiv Al - OH^{-1/2} + F^-(aq) + H^+(aq) \leftrightarrow \equiv AlF^{-1/2} + H_2O(l) \quad (4)$$

$$2 \equiv Ti - OH^{+1/2} + AsO_4^{3-}(aq) + 2H^+(aq) \leftrightarrow \equiv Ti_2O_2^2AsO_2^{-2} + 2H_2O(l) \quad (5)$$

$$\equiv La - OH^{-1/2} + F^-(aq) + 2H^+(aq) \leftrightarrow \equiv LaFH + H_2O(l) \quad (6)$$

As shown in Table S2, the adsorption constants (log*K*) were obtained by best fitting the experimental data to the model calculation values. It is noted that the CD-MUSIC model satisfactorily simulated the adsorption envelopes of As(V) and F^- on meso-Fe/Al and meso-Ti/La with increasing pH values based on the above assumption of four surface species (Fig. 10). Our fitting results indicate that the adsorption mechanism of As(V) dominantly involved the formation of binuclear bidentate surface complexes, whereas F^- was bound by formation of monodentate surface complexes on meso-Fe/Al and meso-Ti/La.

CONCLUSIONS

In summary, four mesoporous metallic oxides (MBOs) with varying components (Fe, Al, Ti, and La) were synthesized through the evaporation-induced self-assembly (EISA) method. These MBOs possessed high surface areas and well-defined pore structures. Adsorption tests for co-uptake of As and F^- indicated that these MBOs have high affinity towards both As and F^-, and the maximum adsorption capacities of meso-Ti/La were as high as 81.42 mg g^{-1} and 44.37 mg g^{-1} for As and F^-, respectively, much higher than those of other bimetallic oxides as reported previously. The adsorption envelopes of As(V) and F^- on meso-Fe/Al and meso-Ti/La in a 1 mg L^{-1} As(V) + 10 mg L^{-1} F^- system can be well stimulated by the CD-MUSIC model with the assumption of four surface species ($\equiv(FeO)_2AsO_2$, $\equiv(TiO)_2AsO_2$, ≡AlF and ≡LaFH). This means that these MBOs could be potential candidates in high-efficiency decontamination of As and F^--containing wastewaters at environmental pH ranges.

ACKNOWLEDGEMENTS

The work was partially supported by NSFC (51002080, 41501197), Natural Science Foundation of Jiangsu Province of China (BK20150915), SPITP (2017103000295, 201410300139), Top-notch Academic Programs Project of Jiangsu Higher Education Institutions (PPZY2015C222) and the Priority Academic Program Development of Jiangsu Higher Education Institutions (PAPD).

Supporting Information

Supporting information may be found in the online version of this article.

REFERENCES

1 Fox KR and Sorg TJ, Controlling arsenic, fluoride, and uranium by point-of-use treatment. *J Am Water Works Ass* **79**:81–84 (1987).
2 Jing CY, Cui JL, Huang YY and Li AG, Fabrication, characterization, and application of a composite adsorbent for simultaneous removal of arsenic and fluoride. *ACS Appl Mater Interfaces* **4**:714–720 (2012).
3 Jadhav SV, Bringas E, Yadav GD, Rathod VK, Ortiz I and Marathe KV, Arsenic and fluoride contaminated groundwaters: a review of current technologies for contaminants removal. *J Environ Manage* **162**:306–325 (2015).
4 Bibi S, Kamran MA, Sultana J and Farooqi A, Occurrence and methods to remove arsenic and fluoride contamination in water. *Environ Chem Lett* **15**:125–149 (2017).
5 Gomez ML, Blarasin MT and Martinez DE, Arsenic and fluoride in a loess aquifer in the central area of Argentina. *Environ Geol* **57**:143–155 (2009).
6 Wang YX, Shvartsev SL and So CL, Genesis of arsenic/fluoride-enriched soda water: a case study at Datong, northern China. *Appl Geochem* **24**:641–649 (2009).
7 Kumar M, Das A, Das N, Goswami R and Singh UK, Co-occurrence perspective of arsenic and fluoride in the groundwater of Diphu, Assam, northeastern India. *Chemosphere* **150**:227–238 (2016).
8 Gonzalez-Horta C, Ballinas-Casarrubias L, Sanchez-Ramirez B, Ishida MC, Barrera-Hernandez A, Gutierrez-Torres D *et al.*, A concurrent exposure to arsenic and fluoride from drinking water in Chihuahua, Mexico. *Int J Environ Res Public Health* **12**:4587–4601 (2015).
9 Farooqi A, Masuda H and Firdous N, Toxic fluoride and arsenic contaminated groundwater in the Lahore and Kasur districts, Punjab, Pakistan and possible contaminant sources. *Environ Pollut* **145**:839–849 (2007).
10 Wang SX, Wang ZH, Cheng XT, Li J, Sang ZP, Zhang XD *et al.*, Arsenic and fluoride exposure in drinking water: children's IQ and growth in Shanyin county, Shanxi province, China. *Environ Health Persp* **115**:643–647 (2007).
11 Jiang SF, Su J, Yao SQ, Zhang YS, Cao FY, Wang F *et al.*, Fluoride and arsenic exposure impairs learning and memory and decreases mGluR5 expression in the hippocampus and cortex in rats. *Plos ONE* **9**:e96041 (2014).
12 Zhu YP, Xi SH, Li MY, Ding TT, Liu N, Cao FY *et al.*, Fluoride and arsenic exposure affects spatial memory and activates the ERK/CREB signaling pathway in offspring rats. *Neurotoxicology* **59**:56–64 (2017).
13 Xi BD, Wang XW, Liu WJ, Xia XF, Li DS, He LS *et al.*, Fluoride and arsenic removal by Nanofiltration technology from groundwater in rural areas of China: performances with membrane optimization. *Sep Sci Technol* **49**:2642–2649 (2014).
14 Huang PP, Cao CY, Wei F, Sun YB and Song WG, MgAl layered double hydroxides with chloride and carbonate ions as interlayer anions for removal of arsenic and fluoride ions in water. *RSC Adv* **5**:10412–10417 (2015).
15 Garcia-Gomez C, Rivera-Huerta ML, Almazan-Garcia F, Martin-Dominguez A, Romero-Soto IC, Burboa-Charis VA *et al.*, Electrocoagulated metal hydroxide sludge for fluoride and arsenic removal in aqueous solution: characterization, kinetic, and equilibrium studies. *Water Air Soil Pollut* **227**:96 (2016).
16 Guzman A, Nava JL, Coreno O, Rodriguez I and Gutierrez S, Arsenic and fluoride removal from groundwater by electrocoagulation using a continuous filter-press reactor. *Chemosphere* **144**:2113–2120 (2016).
17 Brunson LR and Sabatini DA, An evaluation of fish bone char as an appropriate arsenic and fluoride removal Technology for Emerging Regions. *Environ Eng Sci* **26**:1777–1784 (2009).
18 Mlilo TB, Brunson LR and Sabatini DA, Arsenic and fluoride removal using simple materials. *J Environ Eng-Asce* **136**:391–398 (2010).
19 Tang YL, Wang JM and Gao NY, Characteristics and model studies for fluoride and arsenic adsorption on goethite. *J Environ Sci-China* **22**:1689–1694 (2010).
20 Kumar V, Talreja N, Deva D, Sankararamakrishnan N, Sharma A and Verma N, Development of bi-metal doped micro- and nano multi-functional polymeric adsorbents for the removal of fluoride and arsenic(V) from wastewater. *Desalination* **282**:27–38 (2011).
21 Daughney CJ, Fakih M and Chatellier X, Progressive sorption and oxidation/hydrolysis of Fe(II) affects cadmium immobilization by bacteria-iron oxide composites. *Geomicrobiol J* **28**:11–22 (2011).
22 Guo HM, Yang LJ and Zhou XQ, Simultaneous removal of fluoride and arsenic from aqueous solution using activated red mud. *Sep Sci Technol* **49**:2412–2425 (2014).
23 Bibi S, Farooqi A, Hussain K and Haider N, Evaluation of industrial based adsorbents for simultaneous removal of arsenic and fluoride from drinking water. *J Clean Prod* **87**:882–896 (2015).
24 Ju JW, He Z, Liu RP, Liu HJ, Zhang XW and Qu JH, Reusability of Al-F hydroxide precipitates generated in adsorption and coagulation treatment of fluoride for adsorptive removal of arsenic. *Environ Eng Sci* **32**:613–621 (2015).
25 Liu RP, Zhu LJ, He Z, Lan HC, Liu HJ and Qu JH, Simultaneous removal of arsenic and fluoride by freshly-prepared aluminum hydroxide. *Colloid Surface A* **466**:147–153 (2015).
26 Yan L, Tu HW, Chan TS and Jing CY, Mechanistic study of simultaneous arsenic and fluoride removal using granular TiO2-La adsorbent. *Chem Eng J* **313**:983–992 (2017).
27 Phillips DH, Sen Gupta B, Mukhopadhyay S and Sen Gupta AK, Arsenic and fluoride removal from contaminated drinking water with Haix-Fe-Zr and Haix-Zr resin beads. *J Environ Manage* **215**:132–142 (2018).
28 Kazi TG, Brahman KD, Baig JA and Afridi HI, A new efficient indigenous material for simultaneous removal of fluoride and inorganic arsenic species from groundwater. *J Hazard Mater* **357**:159–167 (2018).
29 Waychunas GA, Kim CS and Banfield JF, Nanoparticulate iron oxide minerals in soils and sediments: unique properties and contaminant scavenging mechanisms. *J Nanopart Res* **7**:409–433 (2005).
30 Li FH, Fu H, Zhai JP and Li Q, Synthesis of mesostructured ferric oxyhydroxides templated by alkyl surfactants: effect of pH, F- and solvents, and their adsorption isotherms for As(V). *Micropor Mesopor Mater* **123**:177–184 (2009).
31 Deng SB, Li ZJ, Huang J and Yu G, Preparation, characterization and application of a Ce-Ti oxide adsorbent for enhanced removal of arsenate from water. *J Hazard Mater* **179**:1014–1021 (2010).
32 Li FH, Fu XR, Huang J and Zhai JP, Synthesis of mesostructured iron oxides with potential As(V) adsorption application. *Chem Res Chinese U* **28**:559–562 (2012).
33 Li FH, Layer-by-layer loading iron onto mesoporous silica surfaces: synthesis, characterization and application for As(V) removal. *Micropor Mesopor Mater* **171**:139–146 (2013).
34 Peng N, Wang KF, Liu GG, Li FH, Yao K and Lv WY, Quantifying interactions between propranolol and dissolved organic matter (DOM) from different sources using fluorescence spectroscopy. *Environ Sci Pollut Res* **21**:5217–5226 (2014).
35 Yang PD, Zhao DY, Margolese DI, Chmelka BF and Stucky GD, Generalized syntheses of large-pore mesoporous metal oxides with semicrystalline frameworks. *Nature* **396**:152–155 (1998).
36 Ji HS, Wu WH, Li FH, Yu XX, Fu JJ and Jia LY, Enhanced adsorption of bromate from aqueous solutions on ordered mesoporous Mg-Al layered double hydroxides (LDHs). *J Hazard Mater* **334**:212–222 (2017).
37 Jing CY, Liu SQ, Patel M and Meng XG, Arsenic leachability in water treatment adsorbents. *Environ Sci Technol* **39**:5481–5487 (2005).
38 Stachowicz M, Hiemstra T and van Riemsdijk WH, Multi-competitive interaction of As(III) and As(V) oxyanions with Ca2+, Mg2+, PO43-, and CO32- ions on goethite. *J Colloid Interf Sci* **320**:400–414 (2008).
39 Sadaoka Y, Aono H, Traversa E and Sakamoto M, Thermal evolution of nanosized LaFeO3 powders from a heteronuclear complex, La[Fe(CN)(6)]center dot nH(2)O. *J Alloys Compd* **278**:135–141 (1998).
40 Biswas K, Saha SK and Ghosh UC, Adsorption of fluoride from aqueous solution by a synthetic iron(III)-aluminum(III) mixed oxide. *Ind Eng Chem Res* **46**:5346–5356 (2007).
41 Goldberg S, Application of surface complexation models to anion adsorption by natural materials. *Environ Toxicol Chem* **33**:2172–2180 (2014).

42 Hong HJ, Yang JS, Kim BK and Yang JW, Arsenic removal behavior by Fe-Al binary oxide: thermodynamic and kinetic study. *Sep Sci Technol* **46**:2531–2538 (2011).
43 Zhang YX and Jia Y, Fluoride adsorption onto amorphous aluminum hydroxide: roles of the surface acetate anions. *J Colloid Interf Sci* **483**:295–306 (2016).
44 Kang DJ, Yu XL, Tong SR, Ge MF, Zuo JC, Cao CY *et al.*, Performance and mechanism of Mg/Fe layered double hydroxides for fluoride and arsenate removal from aqueous solution. *Chem Eng J* **228**:731–740 (2013).
45 Waychunas GA, Jun Y-S, Eng PJ, Ghose SK and Trainor TP, Anion sorption topology on hematite: comparison of arsenate and silicate, in *Adsorption of Metals by Geomedia II: Variables, Mechanisms, and> Model Applications*, ed by Mark OB and Douglas BK. Elsevier, Amsterdam, Netherlands, pp. 31–65 (2007).
46 Cui YS and Weng LP, Arsenate and phosphate adsorption in relation to oxides composition in soils: LCD modeling. *Environ Sci Technol* **47**:7269–7276 (2013).
47 Li FH, Geng D and Cao Q, Adsorption of As(V) on aluminum-, iron-, and manganese-(oxyhydr)oxides: equilibrium and kinetics. *Desalin Water Treat* **56**:1829–1838 (2015).
48 Wu X, Zhang Y, Dou X and Yang M, Fluoride removal performance of a novel Fe-Al-Ce trimetal oxide adsorbent. *Chemosphere* **69**:1758–1764 (2007).
49 Liu H, Deng SB, Li ZJ, Yu G and Huang J, Preparation of Al-Ce hybrid adsorbent and its application for defluoridation of drinking water. *J Hazard Mater* **179**:424–430 (2010).

